AIAA SciTech Forum
7-11 January 2019, San Diego, California
AIAA Scitech 2019 Forum

10.2514/6.2019-1820

Check for updates

Single-Laser Krypton Tagging Velocimetry (KTV) Investigation of Air and N_2 Boundary-Layer Flows Over a Hollow Cylinder in the Stevens Shock Tube

M. A. Mustafa* D. Shekhtman† N. J. Parziale‡
Stevens Institute of Technology, Hoboken, NJ 07030, USA

Results are presented for a single-laser Krypton Tagging Velocimetry (KTV) scheme applied to the flow over a hollow cylinder in a shock tube. This scheme is comparatively simpler and cheaper to implement than previous dual-laser schemes and maintained an SNR of $\approx$ 2 in these experiments. Results are presented for experiments performed in 99% N_2/1% Kr and 75% N_2/5% Kr/20% O_2 with Reynolds numbers ranging from 1e5-1e6. For the first time KTV is implemented in air at a pressure of 19 kPa and in N_2 at 25 kPa. The data points over the cylinder are mapped to corresponding wall-normal locations above a flat plate, which allows for comparison with flat-plate boundary-layer theory. Agreement between theory and experiment is excellent, bringing confidence to the utility of KTV in impulse facilities and at the aforementioned conditions.

Nomenclature

λ_{vac} = Transition wavelength, (nm)
A_{ki} = Einstein coefficient for transition from level k to i, (s^{-1})
E_i = Energy of level i, (cm^{-1})
M = Mach number, (-)
Re^{unit} = Unit Reynolds number, (m^{-1})
Pr = Prandlt number, (-)
γ = Ratio of specific heats, (-)
P = Pressure, (Pa)
T = Temperature, (K)
ρ = Density, (kgm^{-3})
u = Streamwise velocity, (ms^{-1})
η = Similarity variable, (-)
μ = Viscosity, (kg/(ms))
R = Surface radius ,(m)
θ = Misalignment angle, (degrees)
x = Streamwise coordinate, (m)
y = Wall-normal coordinate, (m)
y_w = Wall location from perceived apogee, (mm)
y_m = Measured distance from wall of curved surface, (mm)
y_d = Spanwise distance from wall of curved surface to fluorescence line, (mm)

Subscripts
s = Shock wave
1 = Region 1 (upstream of shock)

*Graduate Student, Mechanical Engineering, Castle Point on Hudson, Hoboken, New Jersey, 07030.
†Graduate Student, Mechanical Engineering, Castle Point on Hudson, Hoboken, New Jersey, 07030.
‡Assistant Professor, Mechanical Engineering, Castle Point on Hudson, Hoboken, New Jersey, 07030, AIAA Senior Member.

2	=	Region 2 (downstream of shock, freestream)
3	=	Region 3 (contact surface)
4	=	Region 4 (driver section)
w	=	Wall

I. Introduction

High speed flow is characterized by various complex phenomena such as shock waves, turbulence, chemical reactions and non-equilibrium effects. These phenomena interact with each other, giving rise to additional time and length scales. These complex phenomena and their interactions have design implications for the acceptable aerothermodyanmic loads of a vehicle. Consequently, in order to optimize the design of such vehicles, it is necessary to develop non-intrusive experimental techniques that can accurately measure flow field parameters.

Two ubiquitous velocimetry techniques are Laser Doppler Velocimetry (LDV) and Particle Image Velocimetry (PIV).[1] These particle-based measurements rely on the assumption that the tracer particles travel identically with the flow. However, the particle response time can be inadequate in low-density flows with short time scales. Loth[2] found that at low densities the Knudsen number of a particle can become large. This represents a fundamental limitation of particle-based techniques because the slip condition at the particle surface culminates in reduced response time. Several researchers[3–5] have examined the response of particles to shock waves in an effort to quantify particle response time. Williams et al.[6] suggest that "particle frequency response analyses based solely on shock response tests may well have overestimated the response to turbulence."

Measurement of velocity fluctuations in high-speed turbulent boundary layers is an example that brings the particle-response time limitation to bear. Lowe et al.[7] asserts that "[s]trong evidence exists that experimental data gathered in high speed flows using particle-based techniques exhibit significant particle lag effects on magnitudes of turbulence quantities." This assertion was based on an experimental LDV campaign in a Mach 2.0 turbulent boundary layer, and the authors made particle-lag corrections to address discrepancies in their data. Recent work by Brooks et al.[8] found that particle-lag effects are more pronounced in the turbulence quantities associated with the wall-normal velocity than the streamwise velocity. This is because the wall-normal velocity fluctuation spectrum is flatter (has more high-frequency content) than its streamwise counterpart.

An attractive alternative to particle-based techniques is tagging velocimetry. Tagging velocimetry[9] is typically performed in gases by tracking the fluorescence of a native, seeded, or synthesized gas. Its advantage over PIV techniques in high-speed facilities is that it is not limited by timing issues associated with tracer injection[10] or reduced particle response at Knudsen and Reynolds numbers[2] characteristic of high-speed wind tunnels. Methods of tagging velocimetry include the VENOM,[11–15] APART,[16–18] RELIEF,[19–23] FLEET,[24,25] STARFLEET,[26] PLEET,[27] argon,[28] iodine,[29,30] sodium,[31] acetone,[32–34] NH[35] and the hydroxyl group techniques,[36–39] among others.[40–45]

To recreate high speed flow conditions various facilities are used depending on the requirements. In this work the focus will be on impulse facilities, which are able to create elevated thermodynamic conditions for short periods of time. These facilities, which include shock tubes and shock tunnels, are used to study flows that would otherwise be difficult to replicate using wind tunnels. Challenges with making measurements in these facilities include timing and in the case of particle based techniques, particle injection as well.[46] Applications of velocimetry in impulse facilities include the impulsively started flow over a cylinder in a shock tube,[47] bow shock measurements in a shock tube,[48] flat plate flow visualization,[49] shocked particle drag measurements[50] and PIV in shock tunnels.[10]

In this work, we focus on a version of tagging velocimetry called Krypton Tagging Velocimetry (KTV), that utilizes krypton as the tracer particle. As an inert gas, krypton can expand the use of tagging velocimetry to cases where the chemical composition of the flow is difficult to prescribe or predict. The excitation scheme used here is a single-laser setup where the fluorescence of the tagged Kr is imaged at successive times. This technique is applied to the flow immediately behind a normal shock (region 2) in the Stevens Shock Tube as a means to investigate the utility of KTV in impulse facilities.

II. Single Laser Excitation Scheme for KTV

In this work, we focus on the use of Kr as a tracer for tagging velocimetry. The use of a metastable noble gas as a tagging velocimetry tracer was first suggested by Mills et al.[51] and Balla and Everheart.[52] The key to the use of Kr as a tracer species for diagnostics are the two-photon transitions that are accessible with commercially available optics and laser systems; there are several two-photon transitions in the ≈190-220 nm range. To date, krypton tagging velocimetry (KTV) has been demonstrated by globally seeding high-speed N_2 flows with 1% Kr and air flows with 5% Kr. Applications include: 1) an underexpanded jet (first KTV demonstration);[53] 2) mean and fluctuating turbulent boundary-layer profiles in a Mach 2.7 flow;[54] 3) seven simultaneous profiles of streamwise velocity and velocity fluctuations in a Mach 2.8 shock-wave/turbulent boundary-layer interaction;[55] 4) the freestream of the large-scale AEDC Hypervelocity Tunnel 9 at Mach 10 and Mach 14;[56] and 5) Mach 2.8 shock-wave/turbulent boundary-layer interactions over 8°, 16°, 24° and 32° wedges.[57] In these experiments, the researchers used a pulsed dye-laser to perform the write step at 214.7 nm to form a write line and photosynthesize the metastable Kr tracer; after a prescribed delay, an additional pulsed dye-laser was used to re-excite the metastable Kr tracer to track displacement. Recently, simplified KTV schemes were developed and demonstrated in an underexpanded jet configuration.[58] These simplified schemes utilized either a dye laser and a laser diode or a single dye laser to create the fluorescence lines. In this work, a single-laser scheme is used to make the KTV measurements.

Following the transitions marked in blue in the energy level diagram in Figure 1 along with the relevant transition data in Table 1 (labeled as A, B, C), the single-laser KTV scheme is performed as follows:

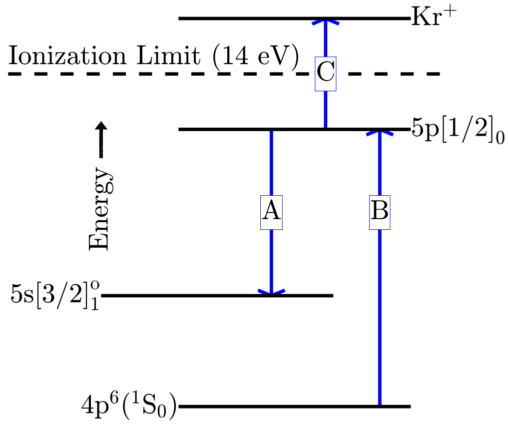

Figure 1: Energy diagram with Racah nl[K]$_J$ notation. Single-Laser Scheme uses excitation at 212.556 nm with successive camera gating (no read laser). Transition details in Table 1.

1. **Write Step:** Excite krypton atoms with a pulsed tunable laser to form the tagged tracer through (2+1) photoionization. Two-photon excitation of $4p^6(^1\mathrm{S}_0) \rightarrow 5p[1/2]_0$ (212.556 nm, transition B) and subsequent one-photon ionization[59] to Kr^+ (212.556 nm, transition C) followed by decay to resonance state $5p[1/2]_0 \rightarrow 5s[3/2]^\circ_1$ (758.95 nm, transition A) and other transitions resulting from Kr^+. The position of the write line is marked by gated imaging of the LIF from these transitions, recorded with a camera positioned normal to the flow.

2. **Read Step:** After a prescribed delay, record the displacement of the tagged krypton by gated imaging of the LIF from the residual $5p[1/2]_0 \rightarrow 5s[3/2]^\circ_1$ (758.9 nm) and Kr^+ transitions.

Table 1: **Relevant NIST Atomic Spectra Database Lines Data, labels match Figure 1. Racah nl[K]$_J$ notation.**

Transition	λ_{vac} (nm)	Nature	A_{ki} (1/s)	E_i (cm^{-1})	E_k (cm^{-1})	Lower Level	Upper Level
A	758.950	Single-Photon	5.1e7	80916.7680	94092.8626	5s[3/2]$^o_1$	5p[1/2]$_0$
B	212.556	Two-Photon	(-)	0	94092.8626	4s^{2}4p^6, ^{1}S$_0$	5p[1/2]$_2$
C	212.556	Single-Photon	(-)	94092.8626	112914.433	5p[1/2]$_2$	Kr$^+$

III. Facilities and Experimental Setup

The experiments were performed in the Stevens Shock Tube, using the single-laser scheme. In this section, we give an overview of the experimental setup and test conditions. The objective is to able to make measurements in the boundary layer behind a normal shock.

The write-laser system for the single laser KTV scheme is a frequency doubled Quanta Ray Pro-350 Nd:YAG laser and a frequency tripled Sirah PrecisionScan Dye Laser (DCM dye, DMSO solvent). The Nd:YAG laser pumps the dye laser with 1000 mJ/pulse at a wavelength of 532 nm. The dye laser is tuned to output a 637.7 nm beam and frequency tripling (Sirah THU 205) of the dye-laser output results in a 212.556 nm beam, with 10 mJ energy, 1350 MHz linewidth and 7 ns pulsewidth at a repetition rate of 10 Hz.

The intensified CCD camera used for all experiments is a Princeton Instruments PIMAX-4 (PM4-1024i-HR-FG-18-P46-CM) with a Nikon NIKKOR 24-85mm f/2.8-4D lens in "macro" mode and positioned approximately 200 mm from the write/read location. The camera gate opens twice: once for 5 ns immediately following the write-laser pulse and again at a prescribed delay time of 500 ns for 50 ns to capture the residual transitions.

A schematic of the Stevens Shock tube is shown in Fig. 2. Three optical windows are placed near the end of the tube where the KTV measurements were made. Fig. 3 shows more detailed views of the driver section and the measurement location. The operation of the shock tube is initiated by a diaphragm-piercing mechanism, consisting of a solenoid and a plunger. Three pressure transducers (P1, P2, P3) are installed along the length of the pipe, two upstream of and one at the optical windows. There is also an additional port used to fill the driven section with the krypton gas mixtures. A hollow cylinder with a sharp edge is installed at the measurement location.

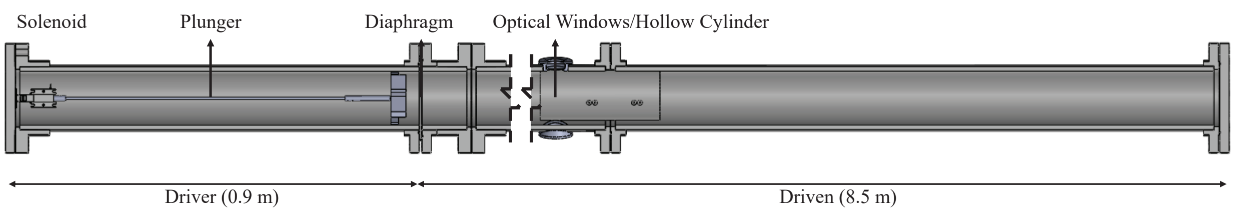

Figure 2: Schematic of Stevens Shock Tube.

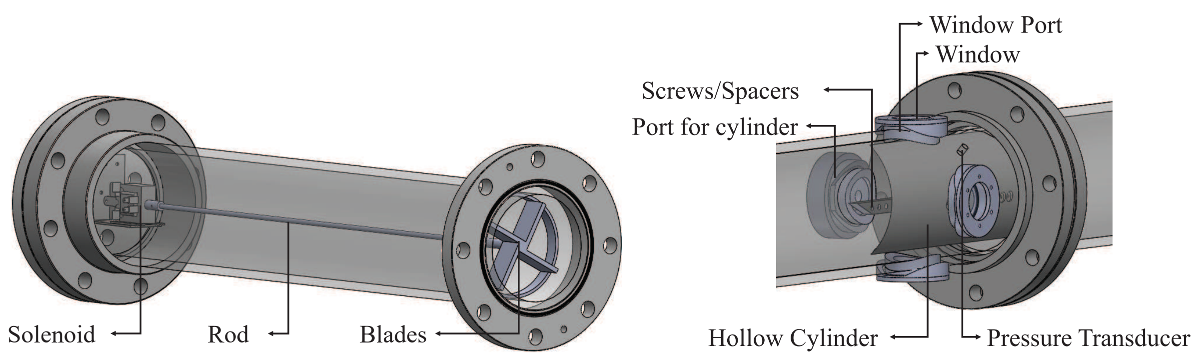

Figure 3: *Left:* Driver section of shock tube. *Right:* Optical windows and hollow cylinder for KTV.

For a calorically-perfect gas, the expected Mach number of the shock wave as a function of the pressure ratio P_4/P_1 and driver/driver gases in a shock tube is,

$$\frac{P_4}{P_1} = \frac{2\gamma_1 M_s^2 - (\gamma_1 - 1)}{\gamma_1 + 1}\left\{1 - \frac{\gamma_4 - 1}{\gamma_1 + 1}\frac{a_1}{a_4}\left(M_s - \frac{1}{M_s}\right)\right\}^{\frac{-2\gamma_4}{\gamma_4 - 1}}. \tag{1}$$

Equation (1) is plotted in Fig. 4 (left) for three different values of a_4/a_1, corresponding to air as the driven gas and air, argon and helium as the driver gas, respectively. Using air as the driver and driven gas, several runs were conducted at several pressure ratios (with the driver at atmospheric pressure) with the goal of shaking down the Stevens Shock Tube. These results appear along the $a_4/a_1 = 1$ line in Fig. 4 (left), and show good agreement with uncertainty predicted as per Moffat,[60]

$$\delta R = \sqrt{\left(\frac{\partial R}{\partial x_1}\delta x_1\right)^2 + \left(\frac{\partial R}{\partial x_2}\delta x_2\right)^2 + \ldots \left(\frac{\partial R}{\partial x_n}\delta x_n\right)^2}. \tag{2}$$

Fig. 4 (right) shows sample pressure traces from an experiment with air as the driver and driven gas and a pressure ratio of $P_4/P_1 \approx 760$. The traces indicate a test time of ≈ 0.5 ms, which is the time between the incident and reflected shock arriving at P3 (this is the transducer installed at the measurement location).

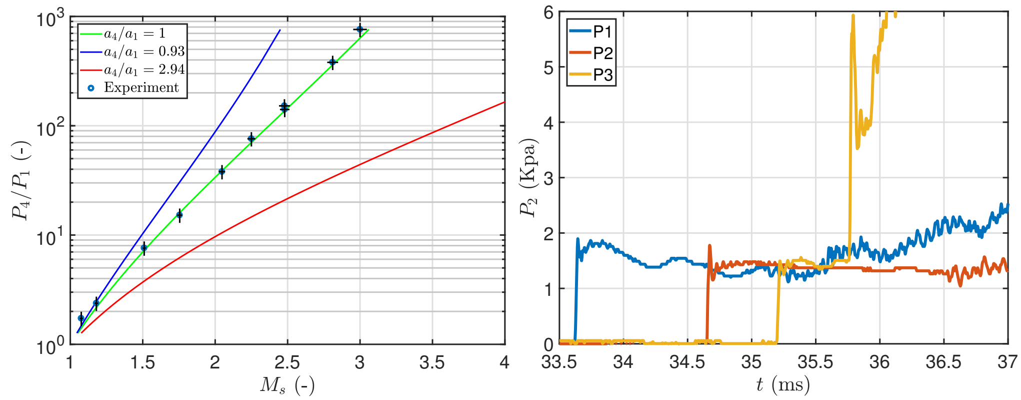

Figure 4: *Left:* Pressure ratio vs shock Mach number. Black bars denote uncertainty. *Right:* Pressure data at shock Mach number of 3. P1, P2 and P3 are the three pressure traducers installed upstream of the measurement location.

The timing of the experiment is designed to keep the lasers at operating temperature. As Fig. 5 shows, the lasers are controlled by a SRS DG 645 pulse generator (PDG 1). This pulse generator is triggered by the combined signal from the SR 560 amplifier (Amplifier 3) and the SRS DG 535 pulse generator (PDG 4). PDG 4 outputs a 10 Hz pulse, and the SRS DG 535 pulse generator outputs a pulse only when the amplified signal of the pressure transducer reaches a certain value. This happens when the shock passes over P3 in the shock tube. Once the amplified P3 signal crosses the threshold, the SRS DG 535 outputs a pulse that triggers the SRS DG 645, which in turn triggers the lasers after a set delay. This allows for making measurements a set time after the shock has passed over while keeping the laser system at operating temperature. The BNC 577 pulse generator is used to activate the solenoid (via a relay) to rupture the diaphragm. The BNC 577 is triggered by the SRS DG 645 with a set delay to ensure that the write laser pulse occurs 90-100 ms after the previous laser pulse.

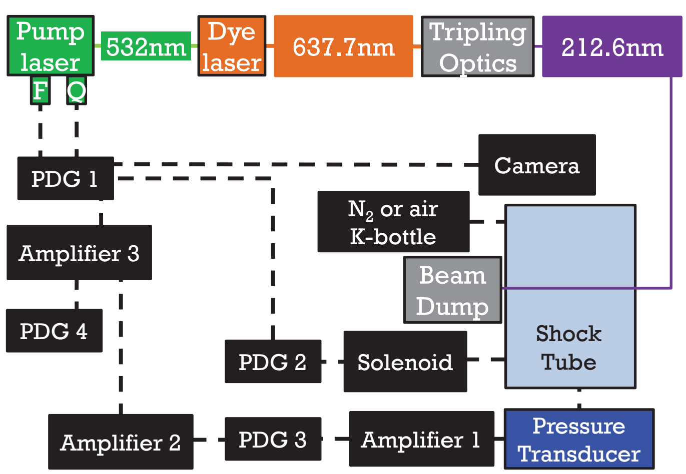

Figure 5: Laser setup and timing for Stevens Shock Tube.

Two gas mixtures were used in the driven section for the experiments. The first was 75% N_2/5% Kr/20% O_2 (air) and the second was 99% N_2/1% Kr (N_2). The driver gas in both cases was helium. The pressure ratio between the driver and driven section was kept fixed at $P_4/P_1 = 380$ and the temperatures were fixed at $\approx$ 298 K. This fixed the shock speed and allowed for a sweep of Reynolds numbers from 1e5-1e6 by changing the pressures proportionately. The run conditions for air are presented in table 2 and the conditions for N_2 are presented in table 3. These calculations were performed using Cantera[61] and the Shock and Detonation toolbox.[62]

Table 2: Experimental Conditions for 75% N_2/20% O_2/5% Kr driven gas mixture and helium as driver gas.

Shot	Re_2^{unit}	M_2	P_2	T_2	ρ_2	u_2	M_s	u_s
(-)	(m^{-1})	(-)	(kPa)	(K)	(kgm^{-3})	(ms^{-1})	(-)	(ms^{-1})
163	2.00e5	1.76	3.46	1450	0.009	1250	4.68	1550
162	3.90e5	1.73	6.37	1360	0.018	1190	4.49	1480
159	7.79e5	1.73	12.7	1360	0.036	1190	4.48	1480
157	1.17e6	1.73	19.1	1360	0.053	1190	4.49	1480

Table 3: Experimental Conditions for 99% N_2/1% Kr driven gas mixture and helium as driver gas.

Shot	Re_2^{unit}	M_2	P_2	T_2	ρ_2	u_2	M_s	u_s
(-)	(m^{-1})	(-)	(kPa)	(K)	(kgm^{-3})	(ms^{-1})	(-)	(ms^{-1})
165	3.86e5	1.71	5.98	1300	0.016	1210	4.36	1510
166	7.85e5	1.73	12.5	1340	0.032	1240	4.45	1550
168	1.17e6	1.72	18.5	1330	0.048	1230	4.43	1540
169	1.67e6	1.73	25.0	1340	0.064	1240	4.46	1540

The boundary layer measurements were made on a hollow cylinder instead of a flat plate. The write laser excited Kr atoms on a line approximately tangent to the cylinder, and the camera captured the projected image of the line and its displacement. The locations of tagged Kr atoms on this cylinder were mapped to corresponding wall-normal points over a flat plate to transform the curved surface problem into a flat plate problem. This method effectively increased the resolution near the wall by stretching the boundary layer. This minimized and sometimes avoided the effect of laser ablation on the test article surface that created large plumes in the fluorescence images which obscured the desired fluorescence lines. Fig. 6 depicts a sketch of a laser beam striking the cylinder (a pipe). The diagram is useful in the calculation of the mapped wall-normal location, y, as a function of the measurement distance y_m (the quantity measured from camera images) from the wall location to an observed point of fluorescence, the radius R of the pipe, the angular offset θ from the true apogee A and the wall location y_w from the observed apogee A^*. The derivation of the mapping expression for y from y_m uses this geometry, beginning with the green and red triangles drawn in the sketch. From the green triangle, a relationship between θ and ϕ is obtained as

$$\sin(\theta + \phi) = \frac{R\sin(\theta) + y_w}{R}. \tag{3}$$

Solving (3) for ϕ,

$$\phi = \arcsin\left(\frac{R\sin(\theta) + y_w}{R}\right) - \theta. \tag{4}$$

In order to find the height of the red triangle, the distance y_d is found via,

$$y_d = \tan(\theta) y_m. \tag{5}$$

Applying the Pythagorean Theorem to the red triangle yields the final expression for the wall-normal distance,

$$y = \sqrt{(R\cos(\theta+\phi) - y_d)^2 + (R\sin(\theta) + y_m + y_w)^2} - R. \tag{6}$$

Figure. 6 shows the effects of cylinder radius (R ranging from pipe size 1 to 6) on the mapping and fig 7 shows the effects of y_w and θ on the mapping from y_m to y. The field of view of the current camera setup allows for a maximum y_m of approximately 15 mm. It is observed that the effect of θ is miniscule until about 20°, but the effects of R and y_w are significant. In these experiments $R = 0.084$ m (size 6 pipe), $y_w \approx 0 - 2$ mm and $\theta \approx 0°$.

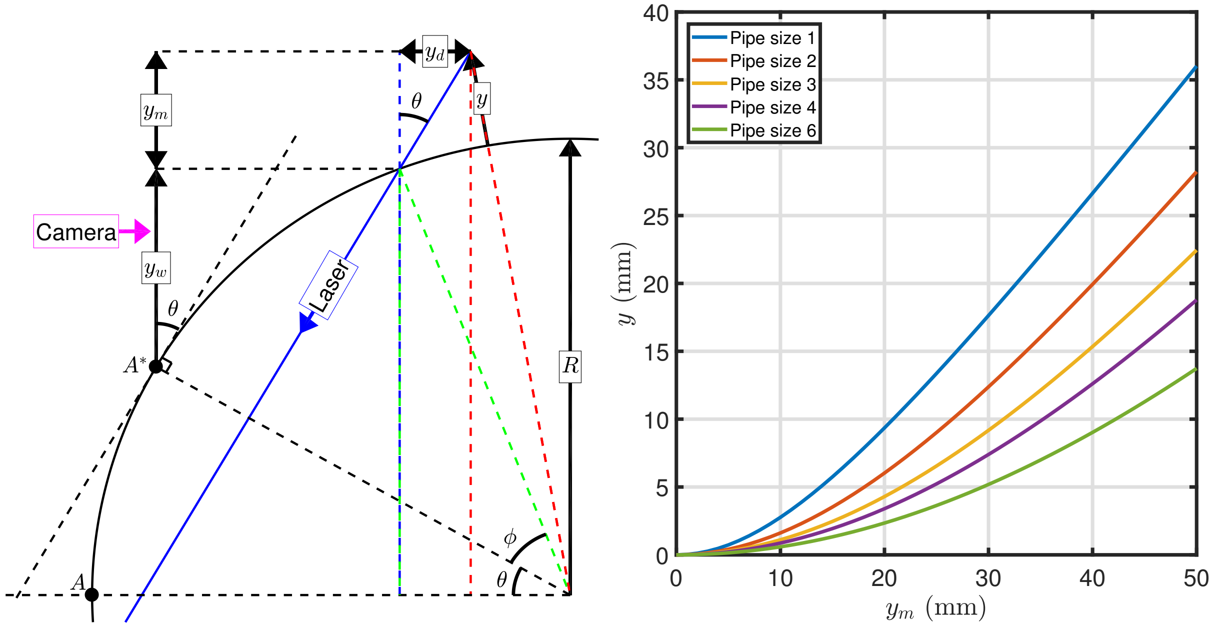

Figure 6: *Left:* Geometry of the cylindrical surface (flow direction is out of the paper). *Right:* Effect of surface radius on mapping.

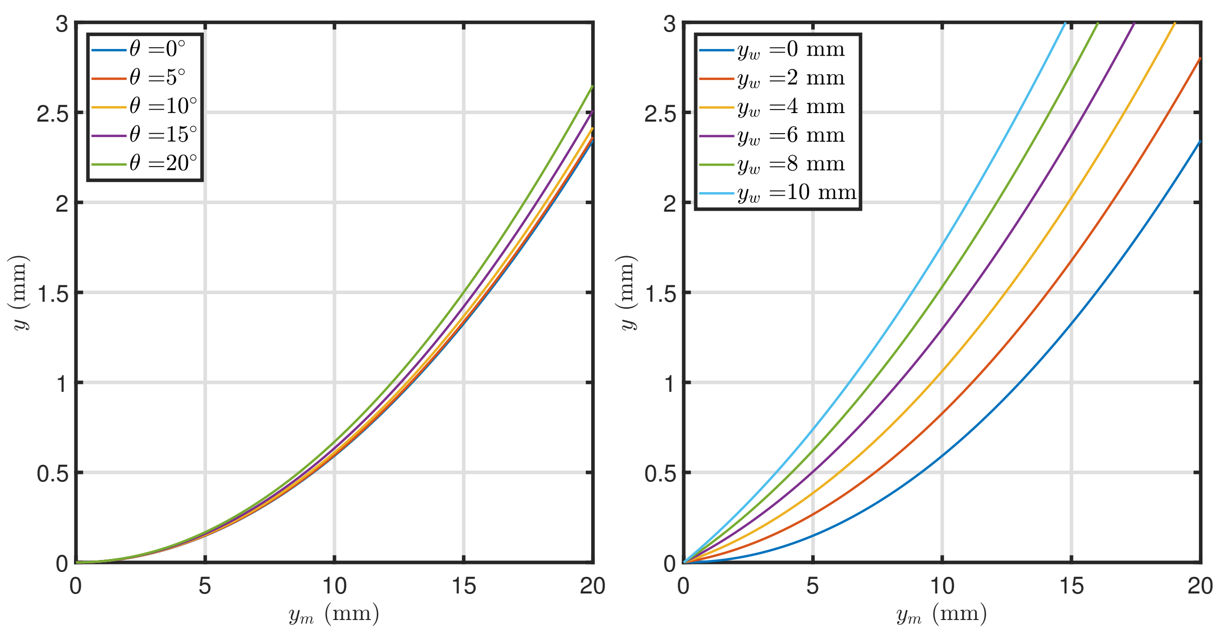

Figure 7: *Left* Effect of y_w on mapping. *Right:* Effect of θ on mapping.

IV. Compressible Laminar Boundary Layer

In this section the compressible boundary-layer theory is presented, the results of which will be compared to the KTV results. The compressible laminar boundary-layer equations over a flat plate are[63]

$$(Cf'')' + ff'' = 0 \tag{7}$$

and

$$(Cg')' + Prfg' = -PrC(\gamma-1)M_2^2 f''^2. \tag{8}$$

Here, $f' = u/u_2$, $g = \rho_2/\rho = T/T_2$, $C = \rho\mu/\rho_2\mu_2$ and the derivatives are with respect to the similarity variable $\eta = \left(\sqrt{u_2}\int_0^y \rho dy\right)/\sqrt{2\rho_2\mu_2 x}$. Following Kuehl,[64] C is evaluated using Sutherland's Law as,

$$C = \frac{C_\mu\sqrt{T_2}}{\mu_2}\frac{\sqrt{g}}{g+(S/T_2)} = C_0\frac{\sqrt{g}}{g+C_1}, \tag{9}$$

where C_μ and S are given in table 4.

Table 4: Constants for Sutherland's viscosity law.

Gas	C_μ	S
Air	1.458e-6	110.4
N_2	1.407e-6	111

With this formulation equations 7 and 8 become,

$$f''' = \frac{g'f''}{g+C_1} - \frac{g'f''}{2g} - \frac{ff''(g+C_1)}{C_0\sqrt{g}} \tag{10}$$

and

$$g'' = \frac{g'^2}{g+C_1} - \frac{g'^2}{2g} - Pr(\gamma-1)M_2^2 f''^2 - \frac{Prfg'(g+C_1)}{C_0\sqrt{g}}. \tag{11}$$

The boundary conditions are $f = f' = 0$ and $g = T_w/T_2$ at $\eta = 0$ and $f' = 1$ and $g = 1$ at $\eta = \infty$. The KTV measurements are made at ≈ 0.043 m from the leading edge.

V. Results

In this section the results for the experiments in air and N_2 are shown. Corresponding flow conditions are listed in tables 2 and 3. To process the KTV exposures, the line centers were found in the following way:
1) Crop the image to an appropriate field of view.
2) Apply a two-dimensional Wiener adaptive-noise removal filter.
3) Convert the images to double precision numbers and normalize the intensity to fall in the range of 0-1.
4) Apply the Gaussian peak finding algorithm from O'Haver[65] to find the line centers for the top row using the read lines in the top row of each image as a first guess.
5) Proceeding from the top-down, apply the Gaussian peak finding algorithm from O'Haver[65] to find the line centers for each row using the line center location immediately above as the guess.
Error bars for the KTV measurements are calculated in the same fashion as Zahradka et al.[54] as

$$\widetilde{U}_{\mathrm{KTV}} = \left[\left(\widetilde{\Delta x}\frac{\partial U}{\partial \Delta x}\right)^2 + \left(\widetilde{\Delta t}\frac{\partial U}{\partial \Delta t}\right)^2 + \left(v'_{RMS}\frac{\partial U}{\partial y}\Delta t\right)^2\right]^{\frac{1}{2}}, \tag{12}$$

where uncertainty estimates of a variable are indicated with a tilde. The results for air are shown in figs. 8,9,10 and 11; and the results for N_2 are shown in figs. 12, 13, 14, and 15. The agreement between the KTV derived velocity profiles and the solutions from boundary-layer theory is excellent. Furthermore, since the profiles should be similar, a collapse of all the KTV velocity profiles is presented in fig. 16 when plotted against the similarity variable η.

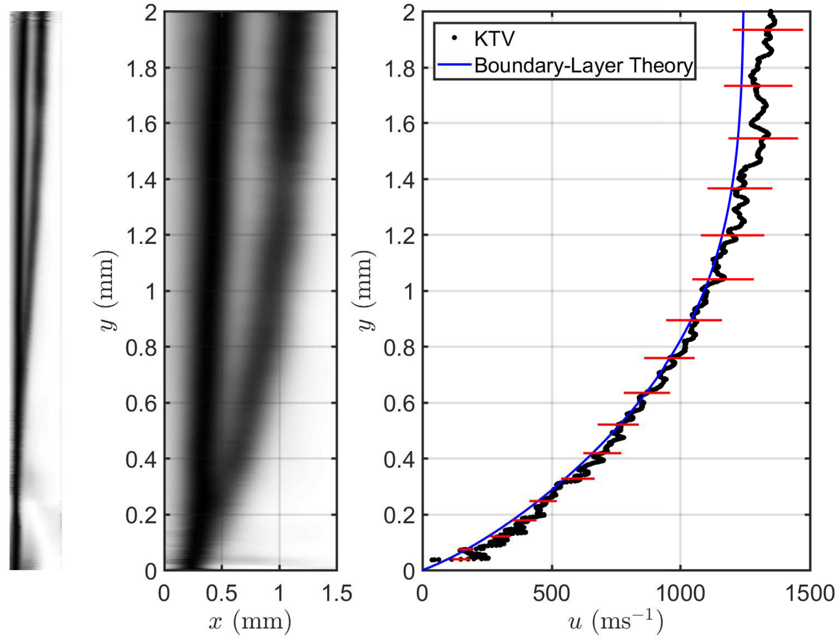

Figure 8: Shot 163 results. *Left:* Superposition of raw write and read KTV images (inverted Scale). *Center:* Superposition of write and read images mapped from y_m to y (black). *Right:* KTV derived velocity profile in black, results from laminar boundary-layer theory in blue and error bars in red.

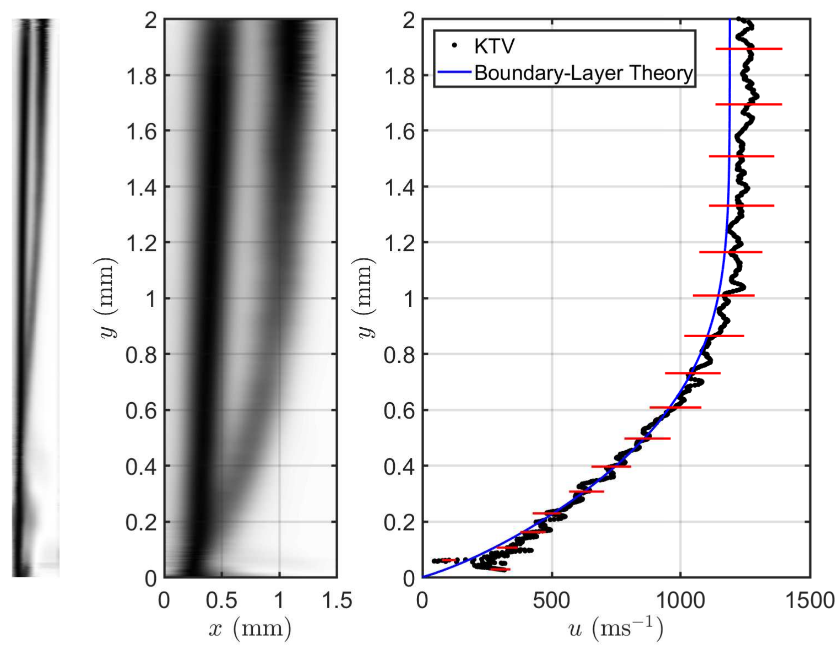

Figure 9: Shot 162 results. *Left:* Superposition of raw write and read KTV images. *Center:* Superposition of write and read images mapped from y_m to y. *Right:* KTV derived velocity profile in black, results from laminar boundary-layer theory in blue and error bars in red.

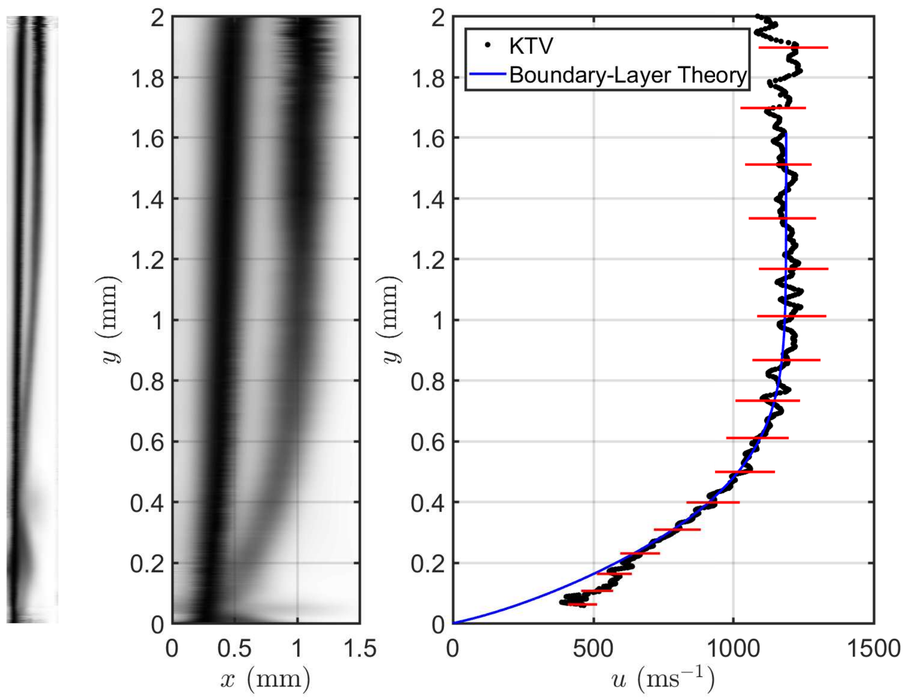

Figure 10: Shot 159 results. *Left:* Superposition of raw write and read KTV images. *Center:* Superposition of write and read images mapped from y_m to y. *Right:* KTV derived velocity profile in black, results from laminar boundary-layer theory in blue and error bars in red.

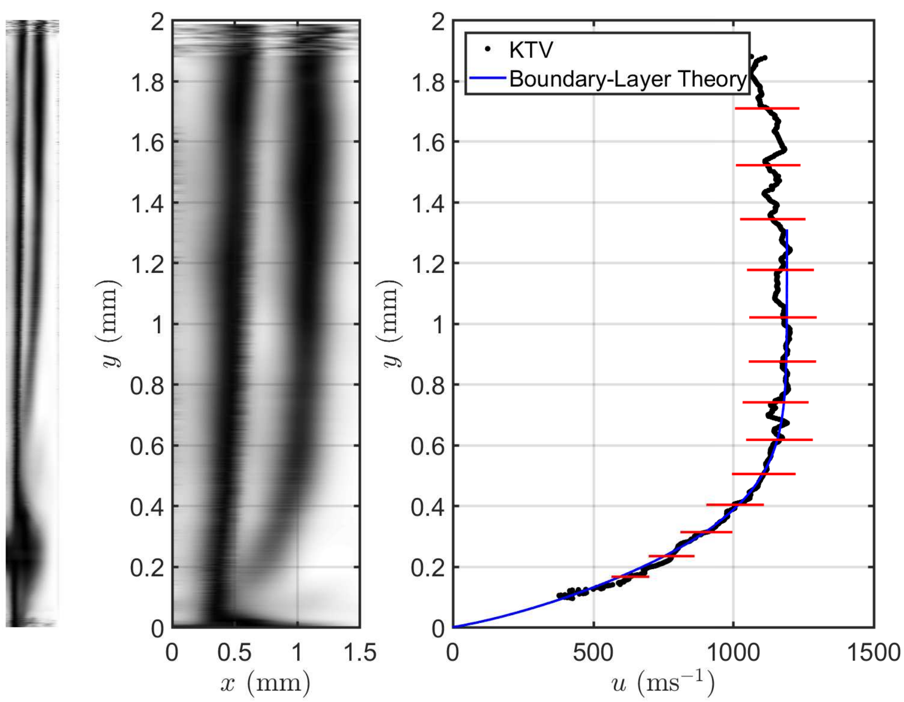

Figure 11: Shot 157 results. *Left:* Superposition of raw write and read KTV images. *Center:* Superposition of write and read images mapped from y_m to y. *Right:* KTV derived velocity profile in black, results from laminar boundary-layer theory in blue and error bars in red.

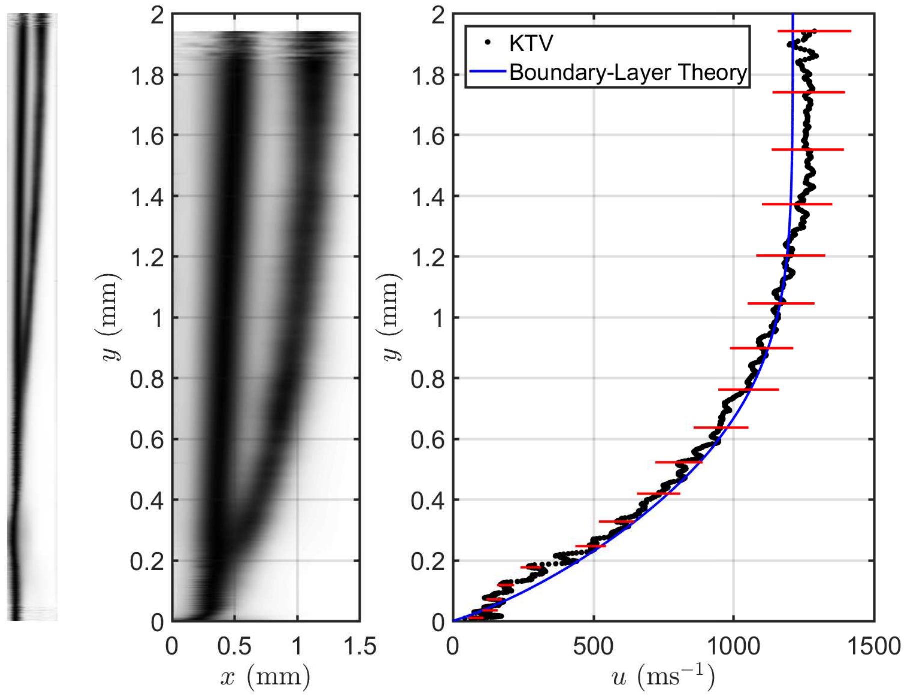

Figure 12: Shot 165 results. *Left:* Superposition of raw write and read KTV images. *Center:* Superposition of write and read images mapped from y_m to y. *Right:* KTV derived velocity profile in black, results from laminar boundary-layer theory in blue and error bars in red.

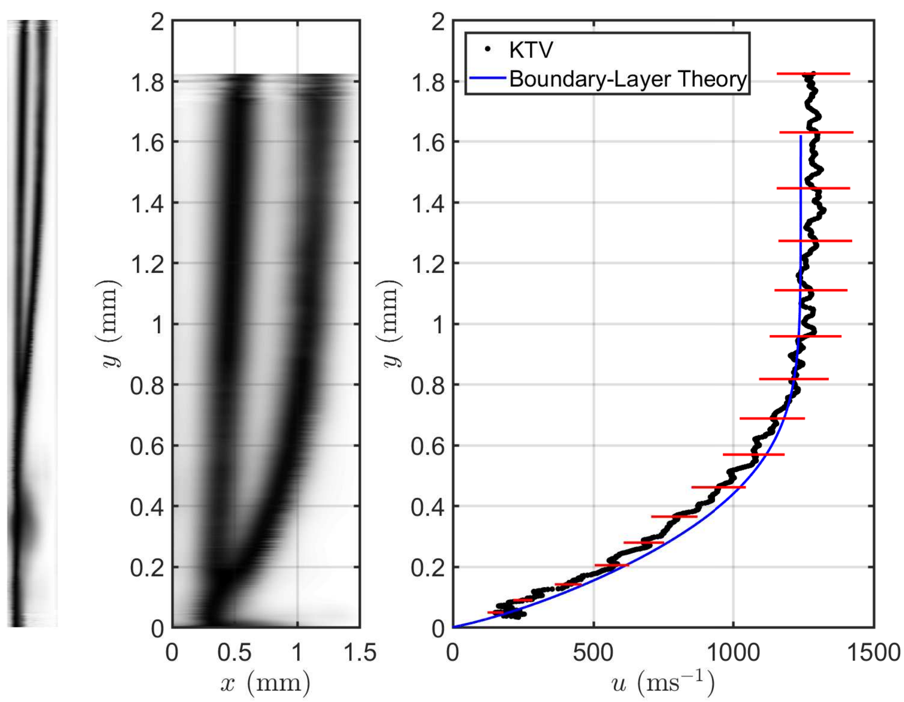

Figure 13: Shot 166 results. *Left:* Superposition of raw write and read KTV images. *Center:* Superposition of write and read images mapped from y_m to y. *Right:* KTV derived velocity profile in black, results from laminar boundary-layer theory in blue and error bars in red.

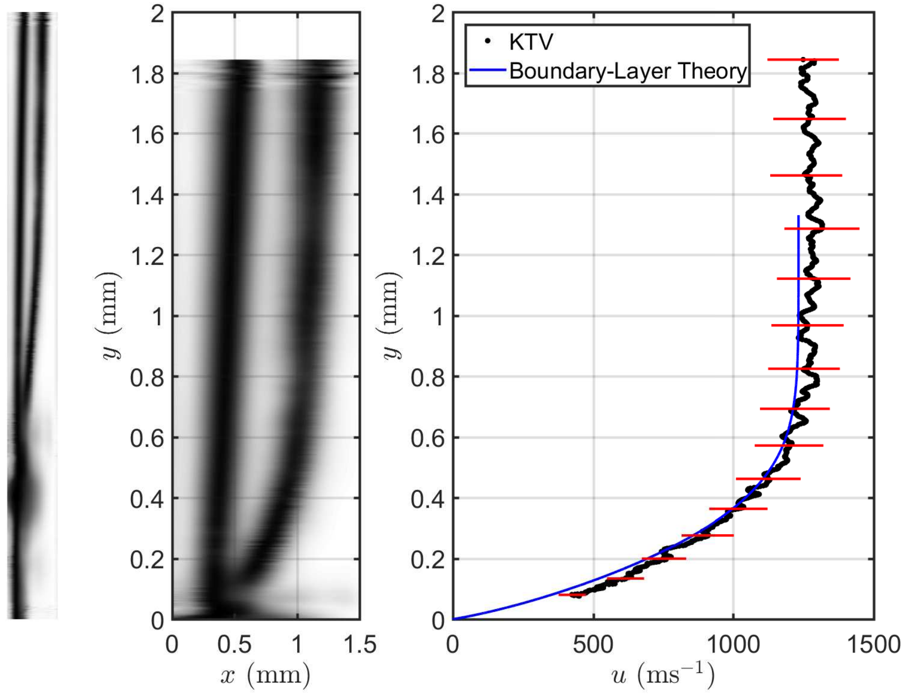

Figure 14: Shot 168 results. *Left:* Superposition of raw write and read KTV images. *Center:* Superposition of write and read images mapped from y_m to y. *Right:* KTV derived velocity profile in black, results from laminar boundary-layer theory in blue and error bars in red.

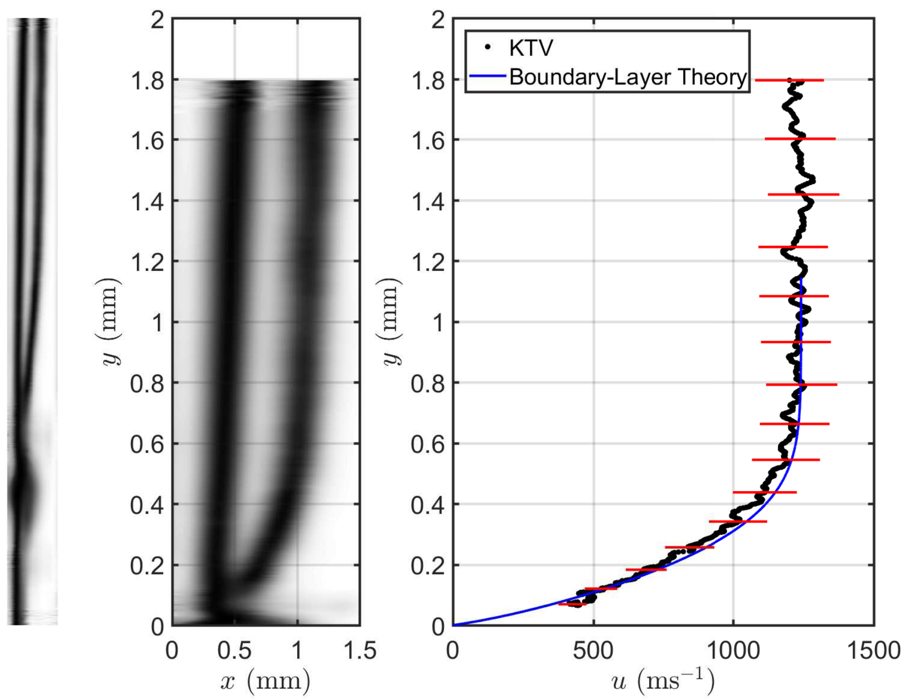

Figure 15: Shot 169 results. *Left:* Superposition of raw write and read KTV images. *Center:* Superposition of write and read images mapped from y_m to y. *Right:* KTV derived velocity profile in black, results from laminar boundary-layer theory in blue and error bars in red.

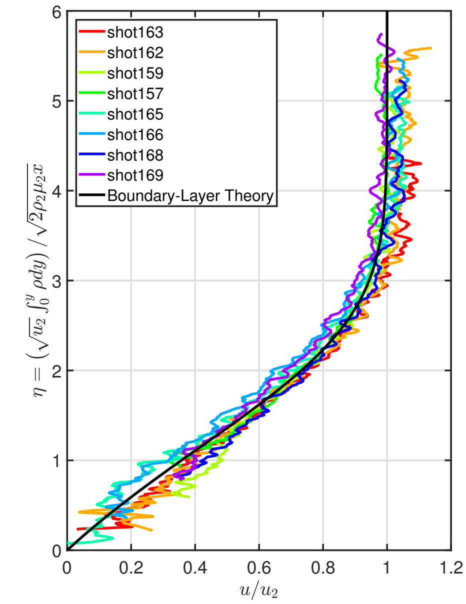

Figure 16: Collapse of KTV derived velocity profiles. Similarity variable η calculated from boundary-layer theory.

VI. Utility of Off-Surface Measurements

In this section, we present an example where off-surface measurements capture flow features that would otherwise be difficult to glean by surface measurements of pressure, temperature and heat transfer. Fig. 17 shows the results of an experiment in the Stevens Shock Tube where $P_2 = 4.7\,\mathrm{kPa}$, $T_2 = 635\,\mathrm{K}$, $u_2 = 613\,\mathrm{ms}^{-1}$ and $M_2 = 1.2$. The KTV derived velocity profile clearly shows that the flow is not established over the hollow cylinder. A possible reason is that the Mach number is not high enough to have an attached shock wave on the sharp-angled cut at the leading edge of the inner surface of the hollow cylinder. Surface measurements may have had more difficulty identifying this behavior. Consequently, to determine whether the desired flow has been established in an experiment, off-surface measurements are invaluable.

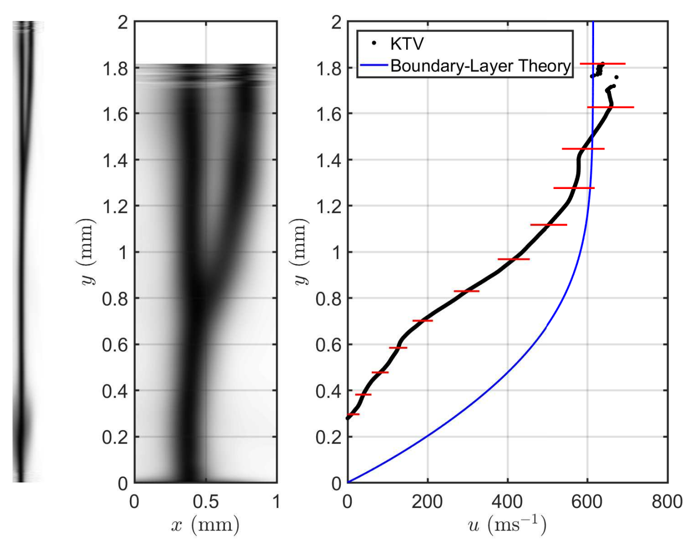

Figure 17: Example of unestablished flow. *Left:* Superposition of raw write and read KTV images. *Center:* Superposition of write and read images mapped from y_m to y. *Right:* KTV derived velocity profile in black, results from laminar boundary-layer theory in blue and error bars in red.

VII. Conclusions

A single-laser KTV setup was used to study the flow behind a normal shock over a hollow cylinder in the Stevens Shock Tube. This single-laser scheme has the advantage of being simpler and cheaper than other two-laser schemes and maintains an SNR of ≈ 2. The scheme utilizes (2+1) photoionization of Kr to create the tracer atoms whose fluorescence is imaged at successive times.

The experiments were performed in the Stevens Shock Tube using helium as the driver gas and air/Kr and N_2/Kr mixtures as the driven gases. The driver and driven pressure ratio was fixed, which allowed for individually varying the Reynolds number from 1e5-1e6 by increasing the pressures proportionately. The experiments in air were performed in pressures of up to 19 kPa and in N_2 up to 25 kPa, both of which are a first for KTV.

A hollow cylinder with a sharp edge was placed in the tube to avoid laser ablation at the surface which created unwanted fluorescence plumes in the field of view. Consequently, the data points over the cylinder were mapped to corresponding wall-normal locations above a flat plate.

The KTV derived velocity profiles were compared to the compressible laminar boundary-layer theory and agreement between the two was excellent. Furthermore, the KTV results collapse to single curve when plotted against the similarity variable. These experiments show the utility of this KTV scheme in making measurements in impulse facilities.

Acknowledgments

Mustafa and Parziale were supported by AFOSR Young Investigator Program Grant FA9550-16-1-0262, and equipment for this work was supported by AFOSR DURIP Grant FA9550-15-1-0325; Ivett Leyva of AFOSR is the Program Manager for both grants. Support was also provided by U.S. Air Force grant (USAF) (FA9101-17-P-0094). Also, we would like to acknowledge the machine work done by Bruce Fraser and Michael DeLorme of Stevens Institute of Technology.

References

[1]Tropea, C., Yarin, A. L., and Foss, J. F., *Springer Handbook of Experimental Fluid Mechanics*, Springer, 2007.

[2]Loth, E., "Compressibility and Rarefaction Effects on Drag of a Spherical Particle," *AIAA Journal*, Vol. 46, No. 9, 2008, pp. 2219–2228. doi: 10.2514/1.28943.

[3]Ragni, D., Schrijer, F.and van Oudheusden, B. W., and Scarano, F., "Particle tracer response across shocks measured by PIV," *Experiments in Fluids*, Vol. 50, No. 1, Jan 2011, pp. 53–64. doi: 10.1007/s00348-010-0892-2.

[4]Elsinga, G. E. and Orlicz, G. C., "Particle imaging through planar shock waves and associated velocimetry errors," *Experiments in Fluids*, Vol. 56, No. 6, Jun 2015, pp. 129. doi: 10.1007/s00348-015-2004-9.

[5]Mitchell, D., Honnery, D., and Soria, J., "Particle relaxation and its influence on the particle image velocimetry cross-correlation function," *Experiments in Fluids*, Vol. 51, No. 4, 2011, pp. 933. doi: 10.1007/s00348-011-1116-0.

[6]Williams, O. J. H., Nguyen, T., Schreyer, A.-M., and Smits, A. J., "Particle response analysis for particle image velocimetry in supersonic flows," *Physics of Fluids*, Vol. 27, No. 7, 2015, pp. 076101. doi: 10.1063/1.4922865.

[7]Lowe, K. T., Byun, G., and Simpson, R. L., "The Effect of Particle Lag on Supersonic Turbulent Boundary Layer Statistics," *Proceedings of AIAA SciTech 2014*, AIAA-2014-0233, National Harbor, Maryland, 2014. doi: 10.2514/6.2014-0233.

[8]Brooks, J. M., Gupta, A. K., Smith, M. S., and Marineau, E. C., "Particle image velocimetry measurements of Mach 3 turbulent boundary layers at low Reynolds numbers," *Experiments in Fluids*, Vol. 59, No. 3, 2018. doi: 10.1007/s00348-018-2536-x.

[9]Koochesfahani, M. M. and Nocera, D. G., "Molecular Tagging Velocimetry," *Springer Handbook of Experimental Fluid Mechanics*, edited by Tropea, C. and Yarin, A. L. and Foss, J. F., Springer, 2007.

[10]Haertig, J., Havermann, M., Rey, C., and George, A., "Particle Image Velocimetry in Mach 3.5 and 4.5 Shock-Tunnel Flows," *AIAA Journal*, Vol. 40, No. 6, 2002, pp. 1056–1060. doi: 10.2514/2.1787.

[11]Hsu, A. G., Srinivasan, R., Bowersox, R. D. W., and North, S. W., "Molecular Tagging Using Vibrationally Excited Nitric Oxide in an Underexpanded Jet Flowfield," *AIAA Journal*, Vol. 47, No. 11, 2009, pp. 2597–2604. doi: 10.2514/1.39998.

[12]Hsu, A. G., Srinivasan, R., Bowersox, R. D. W., and North, S. W., "Two-component molecular tagging velocimetry utilizing NO fluorescence lifetime and NO_2 photodissociation techniques in an underexpanded jet flowfield," *Applied Optics*, Vol. 48, No. 22, 2009, pp. 4414–4423. doi: 10.1364/AO.48.004414.

[13]Sánchez-González, R., Srinivasan, R., Bowersox, R. D. W., and North, S. W., "Simultaneous velocity and temperature measurements in gaseous flow fields using the VENOM technique," *Optics Letters*, Vol. 36, No. 2, 2011, pp. 196–198. doi: 10.1364/OL.36.000196.

[14]Sánchez-González, R., Bowersox, R. D. W., and North, S. W., "Simultaneous velocity and temperature measurements in gaseous flowfields using the vibrationally excited nitric oxide monitoring technique: a comprehensive study," *Applied Optics*, Vol. 51, No. 9, 2012, pp. 1216–1228. doi: 10.1364/AO.51.001216.

[15]Sánchez-González, R., Bowersox, R. D. W., and North, S. W., "Vibrationally excited NO tagging by NO($A^2\Sigma^+$) fluorescence and quenching for simultaneous velocimetry and thermometry in gaseous flows," *Optics Letters*, Vol. 39, No. 9, 2014, pp. 2771–2774. doi: 10.1364/OL.39.002771.

[16]Dam, N., Klein-Douwel, R. J. H., Sijtsema, N. M., and ter Meulen, J. J., "Nitric oxide flow tagging in unseeded air," *Optics Letters*, Vol. 26, No. 1, 2001, pp. 36–38. doi: 10.1364/OL.26.000036.

[17]Sijtsema, N. M., Dam, N. J., Klein-Douwel, R. J. H., and ter Meulen, J. J., "Air Photolysis and Recombination Tracking: A New Molecular Tagging Velocimetry Scheme," *AIAA Journal*, Vol. 40, No. 6, 2002, pp. 1061–1064. doi: 10.2514/2.1788.

[18]Van der Laan, W. P. N., Tolboom, R. A. L., Dam, N. J., and ter Meulen, J. J., "Molecular tagging velocimetry in the wake of an object in supersonic flow," *Experiments in Fluids*, Vol. 34, No. 4, 2003, pp. 531–534. doi: 10.1007/s00348-003-0593-1.

[19]Miles, R., Cohen, C., Connors, J., Howard, P., Huang, S., Markovitz, E., and Russell, G., "Velocity measurements by vibrational tagging and fluorescent probing of oxygen," *Optics Letters*, Vol. 12, No. 11, 1987, pp. 861–863. doi: 10.1364/OL.12.000861.

[20]Miles, R., Connors, J., Markovitz, E., Howard, P., and Roth, G., "Instantaneous profiles and turbulence statistics of supersonic free shear layers by Raman excitation plus laser-induced electronic fluorescence (RELIEF) velocity tagging of oxygen," *Experiments in Fluids*, Vol. 8, No. 1-2, 1989, pp. 17–24. doi: 10.1007/BF00203060.

[21]Miles, R. B., Zhou, D., Zhang, B., and Lempert, W. R., "Fundamental Turbulence Measurements by RELIEF Flow Tagging," *AIAA Journal*, Vol. 31, No. 3, 1993, pp. 447–452. doi: 10.2514/3.11350.

[22]Miles, R. B. and Lempert, W. R., "Quantitative Flow Visualization in Unseeded Flows," *Annual Review of Fluid Mechanics*, Vol. 29, No. 1, 1997, pp. 285–326. doi: 10.1146/annurev.fluid.29.1.285.

[23]Miles, R. B., Grinstead, J., Kohl, R. H., and Diskin, G., "The RELIEF flow tagging technique and its application in engine testing facilities and for helium-air mixing studies," *Measurement Science and Technology*, Vol. 11, No. 9, 2000, pp. 1272–1281. doi: 10.1088/0957-0233/11/9/304.

[24]Michael, J. B., Edwards, M. R., Dogariu, A., and Miles, R. B., "Femtosecond laser electronic excitation tagging for quantitative velocity imaging in air," *Applied Optics*, Vol. 50, No. 26, 2011, pp. 5158–5162. doi: 10.1364/AO.50.005158.

[25]Edwards, M. R., Dogariu, A., and Miles, R. B., "Simultaneous Temperature and Velocity Measurements in Air with Femtosecond Laser Tagging," *AIAA Journal*, Vol. 53, No. 8, 2015, pp. 2280–2288. doi: 10.2514/1.J053685.

[26]Jiang, N., Halls, B. R., Stauffer, H. U., Danehy, P. M., Gord, J. R., and Roy, S., "Selective two-photon absorptive resonance femtosecond-laser electronic-excitation tagging velocimetry," *Optics Letters*, Vol. 41, No. 10, 2016, pp. 2225–2228. doi: 10.1364/OL.41.002225.

[27]Jiang, N., Mance, J. G., Slipchenko, M. N., Felver, J. J., Stauffer, H. U., Yi, T., Danehy, P. M., and Roy, S., "Seedless velocimetry at 100 kHz with picosecond-laser electronic-excitation tagging," *Optics Letters*, Vol. 42, No. 2, 2017, pp. 239–242. doi: 10.1364/OL.42.000239.

[28]Mills, J. L., *Investigation of Multi-Photon Excitation in Argon with Applications in Hypersonic Flow Diagnostics*, Ph.D. thesis, Old Dominion University, 2016.

[29]McDaniel, J. C., Hiller, B., and Hanson, R. K., "Simultaneous multiple-point velocity measurements using laser-induced iodine fluorescence," *Optics Letters*, Vol. 8, No. 1, 1983, pp. 51–53. doi: 10.1364/OL.8.000051.

[30]Balla, R. J., "Iodine Tagging Velocimetry in a Mach 10 Wake," *AIAA Journal*, Vol. 51, No. 7, 2013, pp. 1–3. doi: 10.2514/1.J052416.

[31]Barker, P., Bishop, A., and Rubinsztein-Dunlop, H., "Supersonic velocimetry in a shock tube using laser enhanced ionisation and planar laser induced fluorescence," *Applied Physics B*, Vol. 64, No. 3, 1997, pp. 369–376. doi: 10.1007/s003400050186.

[32]Lempert, W. R., Jiang, N., Sethuram, S., and Samimy, M., "Molecular Tagging Velocimetry Measurements in Supersonic Microjets," *AIAA Journal*, Vol. 40, No. 6, 2002, pp. 1065–1070. doi: 10.2514/2.1789.

[33]Lempert, W. R., Boehm, M., Jiang, N., Gimelshein, S., and Levin, D., "Comparison of molecular tagging velocimetry data and direct simulation Monte Carlo simulations in supersonic micro jet flows," *Experiments in Fluids*, Vol. 34, No. 3, 2003, pp. 403–411. doi: 10.1007/s00348-002-0576-7.

[34]Handa, T., Mii, K., Sakurai, T., Imamura, K., Mizuta, S., and Ando, Y., "Study on supersonic rectangular microjets using molecular tagging velocimetry," *Experiments in Fluids*, Vol. 55, No. 5, 2014, pp. 1–9. doi: 10.1007/s00348-014-1725-5.

[35]Zhang, S., Yu, X., Yan, H., Huang, H., and Liu, H., "Molecular tagging velocimetry of NH fluorescence in a high-enthalpy rarefied gas flow," *Applied Physics B*, Vol. 123, No. 4, 2017, pp. 122. doi: 10.1007/s00340-017-6703-1.

[36]Boedeker, L. R., "Velocity measurement by H_2O photolysis and laser-induced fluorescence of OH," *Optics Letters*, Vol. 14, No. 10, 1989, pp. 473–475. doi: 10.1364/OL.14.000473.

[37]Wehrmeyer, J. A., Ribarov, L. A., Oguss, D. A., and Pitz, R. W., "Flame Flow Tagging Velocimetry with 193-nm H_2O Photodissociation," *Applied Optics*, Vol. 38, No. 33, 1999, pp. 6912–6917. doi: 10.1364/AO.38.006912.

[38]Pitz, R. W., Lahr, M. D., Douglas, Z. W., Wehrmeyer, J. A., Hu, S., Carter, C. D., Hsu, K.-Y., Lum, C., and Koochesfahani, M. M., "Hydroxyl tagging velocimetry in a supersonic flow over a cavity," *Applied Optics*, Vol. 44, No. 31, 2005, pp. 6692–6700. doi: 10.1364/AO.44.006692.

[39]André, M. A., Bardet, P. M., Burns, R. A., and Danehy, P. M., "Characterization of hydroxyl tagging velocimetry for low-speed flows," *Measurement Science and Technology*, Vol. 28, No. 8, 2017, pp. 085202. doi: 10.1088/1361-6501/aa7ac8.

[40]Hiller, B., Booman, R. A., Hassa, C., and Hanson, R. K., "Velocity visualization in gas flows using laser-induced phosphorescence of biacetyl," *Review of Scientific Instruments*, Vol. 55, No. 12, 1984, pp. 1964–1967. doi: 10.1063/1.1137687.

[41]Gendrich, C. P. and Koochesfahani, M. M., "A spatial correlation technique for estimating velocity fields using molecular tagging velocimetry (MTV)," *Experiments in Fluids*, Vol. 22, No. 1, 1996, pp. 67–77. doi: 10.1007/BF01893307.

[42]Gendrich, C. P., Koochesfahani, M. M., and Nocera, D. G., "Molecular tagging velocimetry and other novel applications of a new phosphorescent supramolecule," *Experiments in Fluids*, Vol. 23, No. 5, 1997, pp. 361–372. doi: 10.1007/s003480050123.

[43]Stier, B. and Koochesfahani, M. M., "Molecular tagging velocimetry (MTV) measurements in gas phase flows," *Experiments in Fluids*, Vol. 26, No. 4, 1999, pp. 297–304. doi: 10.1007/s003480050292.

[44]Ribarov, L. A., Wehrmeyer, J. A., Batliwala, F., Pitz, R. W., and DeBarber, P. A., "Ozone Tagging Velocimetry Using Narrowband Excimer Lasers," *AIAA Journal*, Vol. 37, No. 6, 1999, pp. 708–714. doi: 10.2514/2.799.

[45]André, M. A., Burns, R. A., Danehy, P. M., Cadell, S. R., Woods, B. G., and Bardet, P. M., "Development of N_2O-MTV for low-speed flow and in-situ deployment to an integral effect test facility," *Experiments in Fluids*, Vol. 59, No. 1, 2018, pp. 14. doi: 10.1007/s00348-017-2470-3.

[46]Havermann, M., Haertig, J., Rey, C., and George, A., *PIV Measurements in Shock Tunnels and Shock Tubes*, Springer Berlin Heidelberg, Berlin, Heidelberg, 2008, pp. 429–443. doi: 10.1007/978-3-540-73528-1_23.

[47]Wagner, J. L., DeMauro, E. P., Casper, K. M., Beresh, S. J., Lynch, K. P., and Pruett, B. O., "Pulse-burst PIV of an impulsively started cylinder in a shock tube for Re > 105," *Experiments in Fluids*, Vol. 59, No. 6, May 2018, pp. 106. doi: 10.1007/s00348-018-2558-4.

[48]Perkins, A. N., Ramsey, M., and Pitz, R. W., "Investigation of a Bow Shock in a Shock Tube Flow Facility Using Hydroxyl Tagging Velocimetry (HTV)," 49^{th} *AIAA Aerospace Sciences Meeting including the New Horizons Forum and Aerospace Exposition, Aerospace Sciences Meetings*, AIAA-2011-1092, Orlando, Fl, USA, 4-7 January 2011. doi: 10.2514/6.2011-1092.

[49]Danehy, P. M., O'Byrne, S., Houwing, A. F. P., Fox, J. S., and Smith, D. R., "Flow-tagging Velocimetry for Hypersonic Flows using Fluorescence of Nitric Oxide," *AIAA Journal*, Vol. 41, No. 2, 2003, pp. 263–271. doi: 10.2514/2.1939.

[50]Martinez, A. A., Orlicz, G. C., and Prestridge, K. P., "A new experiment to measure shocked particle drag using multi-pulse particle image velocimetry and particle tracking," *Experiments in Fluids*, Vol. 56, No. 1, Nov 2014, pp. 1854. doi: 10.1007/s00348-014-1854-x.

[51]Mills, J. L., Sukenik, C. I., and Balla, R. J., "Hypersonic Wake Diagnostics Using Laser Induced Fluorescence Techniques," *Proceedings of 42nd AIAA Plasmadynamics and Lasers Conference*, AIAA 2011-3459, Honolulu, Hawaii, 2011. doi: 10.2514/6.2011-3459.

[52]Balla, R. J. and Everhart, J. L., "Rayleigh Scattering Density Measurements, Cluster Theory, and Nucleation Calculations at Mach 10," *AIAA Journal*, Vol. 50, No. 3, 2012, pp. 698–707. doi: 10.2514/1.J051334.

[53]Parziale, N. J., Smith, M. S., and Marineau, E. C., "Krypton tagging velocimetry of an underexpanded jet," *Applied Optics*, Vol. 54, No. 16, 2015, pp. 5094–5101. doi: 10.1364/AO.54.005094.

[54]Zahradka, D., Parziale, N. J., Smith, M. S., and Marineau, E. C., "Krypton tagging velocimetry in a turbulent Mach 2.7 boundary layer," *Experiments in Fluids*, Vol. 57, No. 62, 2016. doi: 10.1007/s00348-016-2148-2.

[55]Mustafa, M. A., Hunt, M. B., Parziale, N. J., Smith, M. S., and Marineau, E. C., "Krypton Tagging Velocimetry (KTV) Investigation of Shock-Wave/Turbulent Boundary-Layer Interaction," *Proceedings of AIAA SciTech 2017*, AIAA-2017-0025, Grapevine, Texas, 9-13 January 2017. doi: 10.2514/6.2017-0025.

[56]Mustafa, M. A., Parziale, N. J., Smith, M. S., and Marineau, E. C., "Nonintrusive Freestream Velocity Measurement in a Large-Scale Hypersonic Wind Tunnel," *AIAA Journal*, Vol. 55, No. 10, 2017, pp. 3611–3616. doi: 10.2514/1.J056177.

[57]Mustafa, M. A., , Parziale, N. J., Smith, M. S., and Marineau, E. C., "Amplification and Structure of Streamwise-Velocity Fluctuations in Four Shock-Wave/Turbulent Boundary-Layer Interactions," *Proceedings of AIAA Aviation 2018*, AIAA-2018-3704, Atlanta, Georgia, 25-29 June 2018. doi: 10.2514/6.2018-3704.

[58]Mustafa, M. A. and Parziale, "Simplified read schemes for krypton tagging velocimetry in N_2 and air," *Optics Letters*, Vol. 43, No. 12, 2018, pp. 2909–2912. doi: 10.1364/OL.43.002909.

[59]Miller, J. C., "Two-photon resonant multiphoton ionization and stimulated emission in krypton and xenon," *Physical Review A*, Vol. 40, 1989, pp. 6969–6976. doi: 10.1103/PhysRevA.40.6969.

[60]Moffat, R. J., "Contributions to the Theory of Single-Sample Uncertainty Analysis," *Journal of Fluids Engineering*, Vol. 104, No. 2, 1982, pp. 250–258. doi: 10.1115/1.3241818.

[61]Goodwin, D. G., "An Open-Source, Extensible Software Suite for CVD Process Simulation," *Proceedings of CVD XVI and EuroCVD Fourteen, M Allendorf, F Maury, and F Teyssandier (Eds.)*, 2003, pp. 155–162.

[62]Browne, S., Ziegler, J., and Shepherd, J. E., "Numerical Solution Methods for Shock and Detonation Jump Conditions," GALCIT - FM2006-006, 2006.

[63]White, F., *Viscous Fluid Flow*, McGraw-Hill, 3rd ed., 2006.

[64]Kuehl, J., "Thermoacoustic Interpretation of Second-Mode Instability," *AIAA Journal*, Vol. 56, No. 9, 2018, pp. 3585–3592. doi: 10.2514/1.J057015.

[65]O'Haver, T., *A Pragmatic Introduction to Signal Processing*, University of Maryland at College Park, 1997.